Article

WS₂ Nanotubes as a 1D Functional Filler for Melt Mixing with Poly(lactic acid):Implications for Composites Manufacture

Eimear Magee, Fengzai Tang, Esra Ozdemir, Marc Walker, Tiziana Di Luccio, Julia A. Kornfield, Alla Zak, Reshef Tenne, and Tony McNally*

Cite This: https://doi.org/10.1021/acsanm.2c00489

Read Online

ACCESS | Metrics & More | Article Recommendations | Supporting Information

ABSTRACT: Multi-walled WS₂ nanotubes (NTs) with lengths ranging from 2 to 65 μm and widths from 50 to 110 nm were synthesized in a horizontal quartz-made reactor by a process yielding NTs with aspect ratios (ARs) between ∼40 and >1000. The NTs obtained were thermally stable in air up to 400 °C but were oxidized within the temperature range 400−550 °C to produce yellow WO₃ particles. Critically, 400 °C is well above the temperature used to mix additives with the majority of melt-processable polymers. The hydrophilic WS₂ NTs were easily dispersed in poly(lactic) acid (PLA) using a twin-screw extruder, but the shear stresses applied during melt mixing resulted in chopping of the NTs such that the AR decreased by >95% and the tensile mechanical properties of the PLA were unchanged. Although the as-extruded unfilled PLA was >99% amorphous, the much-shortened WS₂ NTs had a significant effect on the crystallization behavior of PLA, inducing heterogeneous nucleation, increasing the crystallization temperature (T_c) by ∼3 °C and the crystalline content by 15%, and significantly increasing the rate of PLA crystallization, producing smaller and more densely packed spherulites. The reduction in the AR and the nucleating effect of WS₂ NTs for PLA are critical considerations in the preparation, by melt mixing, of composites of rigid 1D NTs and polymers, irrespective of the target application, including bone tissue engineering and bioresorbable vascular scaffolds.

KEYWORDS: WS₂ nanotubes, poly(lactic acid), composites, aspect ratio, melt mixing, crystallization, bioresorbable vascular scaffold
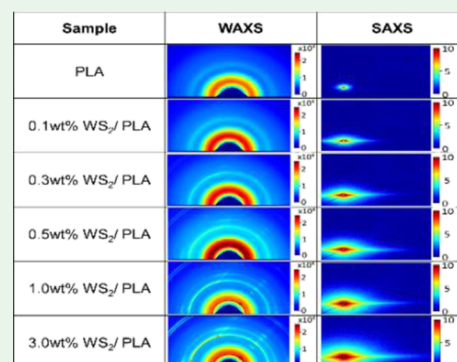
1. INTRODUCTION

Tungsten disulphide (WS₂) nanotubes (NTs) were first reported by Tenne et al[1,2] in 1992, and their synthesis was further developed by NanoMaterials Ltd. through large-scale production by fluidized bed reactor technology. The NTs synthesized then had structures that were highly crystalline and multi-walled, with lengths up to 20 μm and widths between 50 and 150 nm, typically providing aspect ratios (ARs) of 100 or larger.[3] Their synthesis has been largely improved recently via a new horizontal reactor using a perforated quartz reaction chamber.[4] NTs with high crystalline order and ARs as large as 500 and above have been produced. These NTs possess interesting mechanical,[5−7] thermal,[8−10] optical, and electrical[11,12] properties that can benefit a wide range of applications. Additionally, WS₂ NTs have also been shown to be non-toxic and biocompatible.[13−15] Recent developments have also shown the potential of WS₂ NTs for application in energy storage,[16] the medical industry[14,15,17,18] such as a radio-opaque additive for bioresorbable vascular scaffolds,[14] and as a functional filler for polymer composites.[19−22]

Poly(lactic) acid (PLA) is a semicrystalline biopolymer synthesized chemically from bio-derived monomers.[23] It continues to attract intense research interest due to its versatile properties as a biocompatible polymer that has already been exploited in the medical industry as a scaffold material and in biodegradable packaging.[24−27] The family of PLA polymers, depending on the D and L isomer content, can have a range of crystalline contents, which consequently determines the mechanical behavior of the polymer.[28] Various 0D/1D/2D nanomaterials have been used effectively to reinforce PLA, typically at low loadings between 0.5 and 8.0% by weight, and several are known to induce a nucleating effect on the polymer matrix.[29−35]

However, the vast majority of existing studies on composites of polymers and WS₂ NTs to date have been on composites prepared by solution or variations in assisted (e.g., sonication) solution mixing and very few on composites prepared by melt mixing,[19] the latter process being less environmentally contentious, more sustainable, and readily scalable. However, effective dispersion and distribution of most 1D/2D materials in polymer melts is a non-trivial technical challenge. Not only

A

must the thermodynamics of mixing between the 1D/2D material and the polymer of interest be favorable, the shear and extensional forces employed during mixing must be effective in dispersing and distributing, in this instance, WS_2 NTs in the PLA matrix. At the same time, the AR of 1D nanocrystals must be conserved. However, the effect of the forces applied during melt mixing on the AR of the NTs is poorly understood and rarely studied,[36] while it is a relevant factor in reinforcement of the polymer on addition of the 1D filler. Previous related studies paid little attention to the surface chemistry of the WS_2 NTs and to the effect of NT impurities, if present, on the degradation of PLA during melt mixing.

To address this gap in the literature, in this paper, we provide a detailed characterization of the thermal, chemical, and structural properties of the WS_2 NTs used in this study. In particular, we provide a comprehensive analysis from thermogravimetry−mass spectrometry (TGA−MS) studies of a color change of the WS_2 NTs from dark gray/black to yellow/pale green with increasing temperature, a behavior reported once before but not studied in detail.[37] The effect of melt mixing the NTs and PLA in an extruder on the NT AR and consequently on the mechanical properties and the crystallization behavior of PLA is reported.

2. EXPERIMENTAL SECTION

2.1. Materials and Preparation of Composites of PLA and WS_2 NTs. WS_2 NTs were synthesized by Zak's group according to a published procedure;[4] see schematic illustration in Figure S1. PLA (∼98% L-isomer, <2% D-isomer, Ingeo 4032D), Nature Works, was kindly provided by the Kornfield Group, Caltech, USA. Composites of PLA and WS_2 NTs were prepared by melt mixing in a twin-screw extruder with increasing WS_2 NT loading up to 3% by weight. In the first instance, PLA, in a pellet form, was cryo-milled to a powder and dried in a dehumidifying dryer at 80 °C for 4 h. Compositions of PLA and WS_2 NTs in a powder form with various NT weight fractions were weighed and mixed by hand. The compositions were then melt-compounded in a Prism Eurolab 16 mm twin-screw extruder (Thermo Fisher Scientific, USA) with 10 heating zones set from 140 °C at the feed end to 200 °C at the die and a screw speed of 70 rpm to produce pellets of each composite formulation. Gel permeation chromatography (GPC) was used to measure the molecular weight (M_w) of unfilled PLA and the composites of PLA and WS_2 NTs post-extrusion to determine if the polymer degraded during extrusion, either thermally induced or catalyzed by impurities in the WS_2 NTs. The molecular weight (M_w) of the PLA was $1.1 \pm 0.05 \ 10^5$ g/mol and is discussed further below, (see Figure S2), confirming no significant degradation of the polymer with respect to the original as-received PLA pellets.

2.2. Characterization. Scanning electron microscopy (SEM) micrographs were obtained using Zeiss Sigma with an InLens detector at 1−2 kV. All samples were taken from cryo-fractured pellets and sputter-coated using an Au/Pd target prior to imaging. For imaging by transmission electron microscopy (TEM), specimens of PLA and composites of PLA and WS_2 NTs were prepared using a Leica EM FC7 cryo-microtome to cut 80 nm-thick samples, which were transferred on TEM copper grids coated with holey carbon films. The as-received WS_2 NTs were dispersed in ethanol and sonicated for 15 min and then transferred on the same type of TEM holey copper grids. TEM imaging was carried out using a FEI (Thermo Fisher Scientific) Talos F200X system having a X-field emission gun high-brightness electron source and fitted with a Super-X EDS (energy dispersive X-ray spectrometer) system. The EDS system had integrated four silicon drift detectors with a solid angle of 0.9 srad for rapid chemical composition mapping. The microscope was operated at 200 kV throughout the analysis, and the data were acquired using either FEI TIA or Velox software, where appropriate.

In the scanning TEM (STEM) mode, the high-angle annular dark-field image and bright-field (BF) image were taken simultaneously.

TGA−MS of the WS_2 NTs was performed both in air and in N_2 using a Mettler Toledo TGA/DSC1 and a Hiden HPR20 mass spectrometer with a HAL IV interface. The WS_2 NT sample data were obtained for a temperature range of 20−1000 °C at a heating rate of 10 K/min with a purge gas flow rate of 25 mL/min. The electrons were multiplied in a detector via a secondary electron multiplier, which significantly increased the probability of detection of a single ion. The mass scan range was 1−250 Da.

The Raman spectra of the WS_2 NTs were obtained using a Renishaw inVia spectrometer with a 633 nm laser. The equipment was calibrated with monocrystalline silicone samples with a characteristic peak at 520 cm^{-1}. The experiment was performed under ambient conditions using 5% of maximum power to optimize results and avoid thermal or photochemical degradation of the sample.

X-ray photoelectron spectroscopy (XPS) measurements were carried out using a Kratos Axis Ultra DLD spectrometer (Kratos Analytical, Manchester, UK). Samples were mounted on electrically conductive carbon tape upon a sample bar and loaded into the spectrometer. Once a pressure lower than 1×10^{-6} mbar had been reached, the samples were transferred to the main analysis chamber. The samples were illuminated with a monochromated Al Kα X-ray source ($h\nu$ = 1486.7 eV) and flooded with low-energy electrons from a charge neutralizer in order to prevent the surface from becoming positively charged during the experiment. Data were collected at a take-off angle of 90° in a hemispherical analyzer using a pass energy of 160 eV for survey spectra and 20 eV for high-resolution core level spectra (resolution approx. 0.4 eV). Data were analyzed using the CasaXPS software package, using mixed Gaussian−Lorentzian (Voigt) line shapes and Shirley backgrounds. The spectrometer was calibrated using the Ag $3d_{5/2}$ peak and Fermi edge of clean polycrystalline Ag prior to the start of the experiments, with the transmission function being determined using various clean metallic foils. The binding energy scale was calibrated during the analysis, using the C−C/C−H component in the C $1s$ region at 285.0 eV as the reference point.

Differential scanning calorimetry (DSC) was performed using a DSC1 Star instrument (Mettler Toledo, USA). Samples of unfilled PLA and extruded composites of PLA and WS_2 NTs weighing approximately 8 mg were sealed in standard aluminum pans. Heating and cooling cycles were carried out under a nitrogen atmosphere at a flow rate of 50 mL min^{-1}. The samples were heated from 20 to 200 °C, held at 200 °C for 5 min, and cooled to 20 °C using a rate of heating of 10 °C min^{-1} and a cooling rate of 5 °C min^{-1}.

For polarized optical microscopy, samples of PLA and the composites of PLA and WS_2 NTs were cut in 50 μm-thick sections using a Tissue-Tek Cryo3 cryostat microtome after being embedded and frozen in optimal cutting temperature (OTC) embedding material. Samples were placed between microscope slides and (THMS600, Linkam scientific) heated from 20 to 200 °C at 10 °C min^{-1}, held at 200 °C for 5 min, and then cooled to 20 °C at a rate of 10 °C min^{-1} with images being taken every minute, corresponding to 10 °C intervals. Polarized light micrographs (4× magnification) of the PLA and composites were obtained through crossed linear polarizers on a Zeiss Universal microscope equipped with a Canon EOS DS30 camera for image acquisition. Images were taken at equal intervals of sample heating and cooling.

X-ray diffraction (XRD) measurements were performed at room temperature using a third generation Malvern Panalytical Empyrean system equipped with multicore (iCore/dCore) optics and a Pixcel3D detector operating in the 1D scanning mode. A Cu tube was used giving Cu K$_{\alpha1/2}$ radiation (1.5419 Å). All scans were acquired in the range 5−70° 2θ with a step size of 0.131°. Simultaneous wide- and small-angle X-ray scattering (SAXS and WAXS) was measured at APS beamline 5-ID-D at the Argonne National Laboratories. The extruded pellets of PLA and composites of PLA and WS_2 NTs with loadings of 0.1, 0.3, 0.5, 1.0, and 3.0 wt % WS_2 NTs were positioned with their long axis (extrusion direction) perpendicular to the incident X-ray

beam for acquisition in the transmission mode. Diffraction patterns were acquired every 1s at an exposure of 0.1 s for SAXS and 10 s for WAXS, using X-rays with a wavelength of 0.7293 Å, at three different axial positions and averaged afterward. WAXS and SAXS images were acquired on Rayonix CCD detectors with a sample to detector distance of 200.51 and 8.503 mm, respectively. The wavevector, q, had been calibrated using a spinning silicon diffraction grid. The air scattering signal was subtracted from each scan to isolate scattering of the samples with respect to the background.

3. RESULTS AND DISCUSSION

The high shear stresses applied during melt mixing may result in fracture of the rigid WS_2 NTs; therefore, it is critical to characterize extensively the NTs prior to and post-melt mixing with PLA. Moreover, it is also critical to characterize the surface chemistry of the WS_2 NTs and the interfacial interactions between NTs and the NTs and PLA. Figure 1a
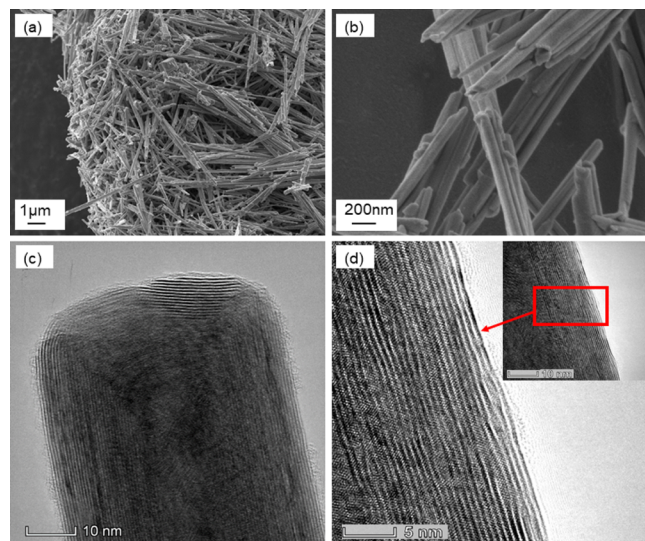

Figure 1. Electron microscopy images of WS_2 NTs. (a,b) SEM images under different magnifications and (c,d) TEM images of two individual NTs, the former showing a closed end.

shows a bundle of WS_2 NTs, and Figure 1b reproduces a detail of Figure 1 under higher magnification where the NTs typically have a diameter of about 50 nm and lengths in the low tens of microns, resulting in ARs up to 1000. The NTs have predominantly a close-ended structure, a consequence of the synthesis method employed. It should be noted that ultrasonication is widely used to disperse WS_2 NTs in solution; however, it has been shown to induce breakage of NTs[20] producing open-ended NT structures, which are observed from microscopy. This also results in much shorter NT lengths and, in turn, reduces the AR of the NTs. The closed ends of the WS_2 NTs used in this study can be clearly seen in the TEM image in Figure 1c.

TEM imaging of the WS_2 NTs also revealed the multi-walled structure of these NTs. The TEM images were analyzed using ImageJ software to determine the width and length of NTs and the number of walls in the multiwall structures and hence the spacing between the walls; see Figure 1c,d. A large range of dimensions was found as the widths of NTs varied from 52 to 110 nm and the lengths varied from 2.45 to 65.6 μm. This large distribution in tube dimensions results in a broad range of NT ARs, as reported previously.[3] Additionally, the number of walls varied from 13 to 28 along the length of the NTs imaged,

but at the closed ends (Figure 1c), the number of walls ranged from 8 to 23. However, it should be noted that while there is some variation in the dimensions of the NTs, the wall spacing between neighboring layers of individual NTs is consistent at approximately 0.65 nm, in agreement with that expected from calculations reported previously.[38] Figure 2 exhibits STEM—EDS analysis used to identify the chemical composition of the NTs, where both W and S were detected within the WS_2 NT structure, as well as oxygen and carbon from airborne contaminants. The electron diffraction pattern (Figure 2c) reveals a multi-helical structure, and the 0002 basal plane and 10−10 and 11−20 prismatic planes are assigned from Miller—Bravais indices. The chirality within a single NT is due to the thickness of the walls altering the magnitude of the strain on the wall curvature and consequently the geometry of the NTs. Hence, incomplete walls within the multi-layered structure leads to a change in NT chirality, a phenomenon determined from the growth process controlling both NT thickness and the number of NT walls.[39] The observation of inconsistencies in the wall structure is important as it is at these positions along the NTs that rupture may occur due to the stresses applied during melt mixing in extruders.

For melt mixing any 0D/1D/2D material with a polymer, it is critical that the filler material is thermally stable at the temperature where the melt mixing process is performed, for example, for PLA, the processing temperature is 200 °C for engineering polymers much higher. Thermal analysis of the WS_2 NTs was performed by TGA in an air atmosphere, Figure 3a), where a total mass loss of ∼8% was detected when the sample was heated to 550 °C, with no further mass loss at higher temperatures, up to 1000 °C. A small mass loss of 1.7% was detected below 400 °C, which can be attributed to evaporation of physisorbed water from the surface, inner core, or in between the layers of the NTs.[40]

A further mass loss of 6.1% was measured between 400 and 550 °C. This weight loss progression as the temperature increased corresponds to the WS_2 oxidation accompanied by a color change of the WS_2 NTs powder from an original black (20 °C) to dark gray (500 °C) and then to a yellow/pale green (800 °C) (see Figure 3a-top). This significant mass loss and color change were not observed in an N_2 atmosphere (see Figure S2) as WS_2 NTs are known to be stable up to more than 1000 °C in an inert atmosphere.[41] TGA—MS analysis of the products evolved during the thermally induced degradation (oxidation) of the WS_2 NTs in the temperature region 400−550 °C shows an endothermic peak, which can be assigned to the elimination of sulfur and absorption of oxygen ions and conversion of WS_2 to WO_3. The difference in molecular weights of two compounds (248 and 232, accordingly) is in good agreement with the obtained mass loss [i.e., (248 − 232)/248 = 6.45 vs 6.1% from TGA]. Moreover, the appearance of the yellow color characteristic of WO_3 confirms this transformation. It can be seen also from the ion evolution profiles that the degradation products containing the same ions (sulfur/oxygen/hydroxyl) follow the same trend, which indicates that the formation/elimination of the products takes place in the same degradation step. The major thermolysis products in Figure 3b were identified as sulfur-containing fragments (m/z = 64, 48, 66, and 50 Da), where the base peak at 64 Da is due to the elimination of both S_2 and SO_2 fragments as they contribute to the intensity of the same peak. Indeed, the possible reaction, oxidation of WS_2 NTs, can be described as $2WS_2 + 7O_2 = 2WO_3 + 4SO_2$.
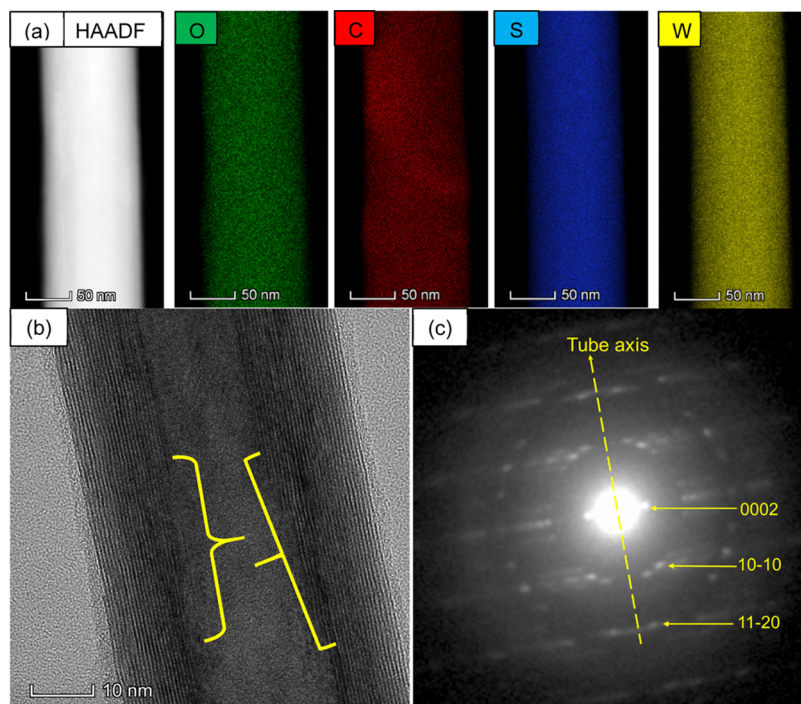
Figure 2. (a) STEM−EDS chemical analysis of WS$_2$ NTs, (b) TEM identification of incomplete NT wall structures, and (c) electron diffraction pattern of the WS$_2$ NTs.
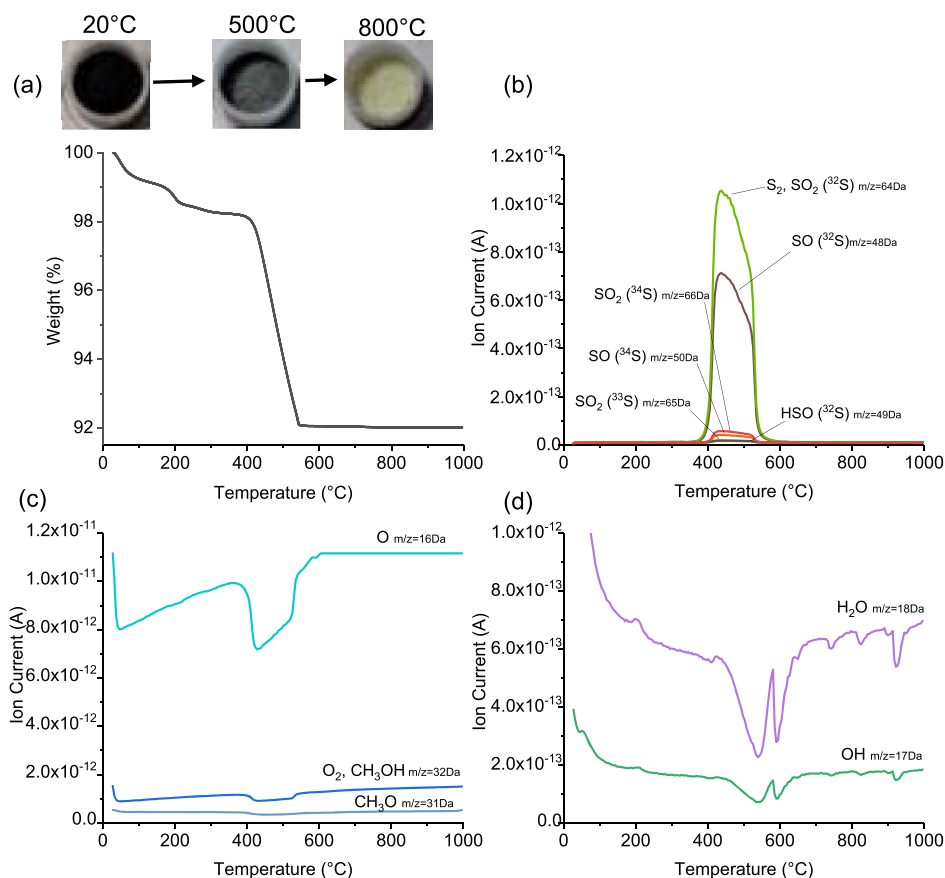

Figure 3. (a) TGA−MS profile for WS$_2$ NTs with corresponding color change through heating and the characteristic ion current curves for WS$_2$ NTs, (b) sulfur-containing major products, (c) oxygen-containing products, and (d) OH-containing products.

Also, the most dominant peaks include ^{32}S isotope peaks, as expected, considering the isotopic abundance of sulfur (^{32}S with the highest abundance of 95%), and the fragments with the ^{34}S isotope (abundance of 4%) are less dominant, yet still

exist. As the TGA−MS experiments were performed in air, the primary degradation products could further react with oxygen to form additional bonds. The elimination of sulfur from WS$_2$ NTs in the 400−550 °C temperature range resulted in the formation of additional sulfur species containing oxygen, which can be clearly seen from the SO fragment apparent at 48 Da. Therefore, in this temperature range, the WS$_2$ NTs become completely oxidized and chemical composition changes from an induced sulfide via an oxide reaction to produce a yellow WO$_3$ (WO$_x$ are usually blue or violet) powder. It should be noted that there are insufficient oxygen contaminants within the NT structure to induce oxidation of WS$_2$ within an inert environment.

Raman spectroscopy was used to study the structural/composition changes generated by heating the WS$_2$ NTs to 550 °C (Figure 4).
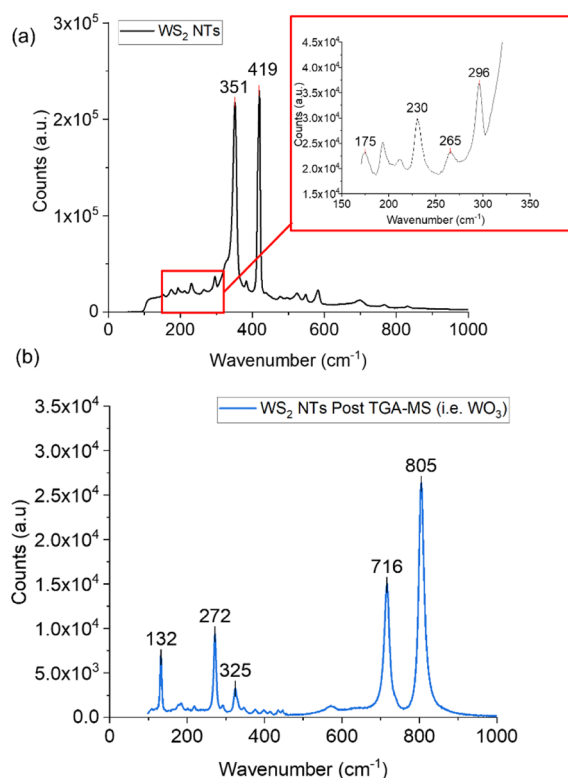

Figure 4. Raman spectra of (a) WS$_2$ NTs prior to thermal treatment and (b) WS$_2$ NTs post-TGA−MS (WO$_3$) analysis.

The main peaks observed in the spectra for the as-received WS$_2$ NTs show the E$_{2g}^1$ and A$_{1g}$ active breathing and vibrational modes. The area of the spectrum expanded and is shown in the inset of Figure 4a, which reveals the acoustic modes E$_{2g}^1$(M) − LA(M); LA(M) (175 cm^{-1}), A$_{1g}$(M) − LA(M) (230 cm^{-1}), 2LA(M) − 3E$_{2g}^2$(M) (265 cm^{-1}), and 2LA(M) − 2E$_{2g}^2$(M) (296 cm^{-1}) shown to be active in WS$_2$ crystal structures.[42] However, due to the backscattering configuration along the surface perpendicular to the c-axis, E$_{1g}$ is forbidden. Also, E$_{2g}^2$ is typically blocked by the notch filter, owing to its low frequency (30 cm^{-1}).[43] Consequently, E$_{2g}^1$ and A$_{1g}$ are the most prominent Raman modes found in the Raman spectra of WS$_2$ NTs. All the measurements are in excellent agreement with the previous literature.[11,43−45] Berkdemir et al.[46] suggested that the overlap of the longitudinal acoustic phonon mode (2LA) is within 5 cm^{-1} of E$_{2g}^1$, leading to a broadened

peak and an increase in intensity of the band at 172 cm^{-1}, which is due to the impact of the number of layers within the NT walls of non-zone-center LA phonons. Additionally, it should be noted that there is a slight increase in the base of the A$_{1g}$ (419 cm^{-1}) peak, which has been described by Staiger et al.[43] to correlate with the emergence of a peak at 416 cm^{-1} associated with the B$_{1u}$ active mode. The B$_{1u}$ mode has been found to be silent in other WS$_2$ structures and incidentally is a unique feature of WS$_2$ NT structures due to the geometrical curvature of the WS$_2$ layers in NTs. Figure 4b shows the Raman spectrum for the yellow powder obtained after heating the sample to 800 °C, where a significantly different Raman spectrum compared to that of neat NTs was obtained, clearly identifying notable changes in the chemical composition and structure. Peaks known to correlate with monoclinic WO$_3$ nanostructures were observed[47,48] with peaks at 132, 272, and 325 cm^{-1} assigned to O−W−O deformation vibrations, and those at 716 and 805 cm^{-1} were attributed to the stretching vibration of O−W−O molecules. This is consistent with the data from the TGA−MS measurements as the WS$_2$ NTs became completely oxidized from the heating process to produce crystalline WO$_3$.

From XRD analysis of the WS$_2$ NTs (Figure 5a), the most intense peak observed was at $2\theta = 14.5°$ corresponding to the
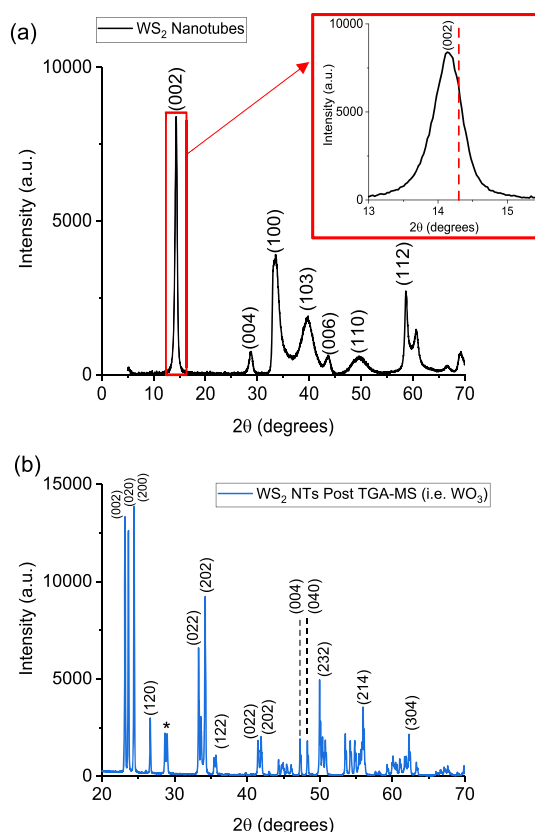

Figure 5. XRD pattern of (a) WS$_2$ NTs and (b) WS$_2$ NTs post-TGA−MS.

(002) crystallographic plane, which is typically a sharp peak associated with the interlayer spacing of the WS$_2$ crystal structure of the NTs. In the inset, the expanded region of the (002) peak of WS$_2$ is shown. This peak is shifted to a lower angle compared to the diffraction peak of 2H-WS$_2$ flakes (red dashed line). This shift shows that the interlayer spacing in the

NTs is larger than that of WS_2 flakes, which was attributed in the past to relaxation of the bending strain in the NTs.[3] Peaks occurring at higher angles, such as those corresponding to (006) and (112) planes, are related to the elongated periodic layered structure of the NT, therefore generating broader and less intense peaks in the spectra.[49,50]

Basal planes such as (101) and (103) have higher intensities and broadened peaks, which identify with the 3D atomic structure of cylindrical NTs, analogous with their carbon NT counterparts, due to the similarity in the nanostructure.[51] Figure 5b shows the XRD profile of the WS_2 NTs post-TGA−MS analysis, clearly identifying a significant change in crystallographic plane alignment. Structural planes were determined using computational analysis, some of which are identified in Figure 5b, corresponding to monoclinic WO_3 nanostructures, with d-spacings of 3.8 Å. It is noteworthy to highlight that in the WO_3 spectra, the peak marked with (*) in Figure 5b overlaps with the (004) and (101) planes ($2\theta = 28.8$ and 33.6°, respectively) of the WS_2 NTs.[52,53] Broadening of these XRD peaks in the WS_2 NTs spectrum is attributed to the submicron sizes of the NTs.

Of critical importance in promoting interfacial interaction between the NTs and PLA is an understanding of the surface chemistry of the NTs. To this end, XPS measurements were also performed to identify the chemical composition of WS_2 NTs pre- and post-TGA−MS, outlined in Table 1, with

Table 1. Elemental Ratio of WS_2 NTs and WS_3 NTs Post-TGA-MS (i.e., WO_3)

sample	Na	O	C	S	W
WS_2	0	7.3	20.0	49.3	23.5
WO_3	4.5	51.3	29.3	0	15.0

corresponding deconvoluted spectral analysis of WS_2 NTs (Figure 6a−d), and for the WO_3 yellow product (Figure 6e−h), the survey spectra are shown in Figure S3. The XPS for WS_2 NTs shows phases identified for tungsten, sulfur, and of airborne impurities such as carbon and oxygen, consistent with the results of the STEM−EDS analysis (Figure 2). Analysis of the chemical composition of the WS_2 NTs from XPS determined 23.5 at. % tungsten and 49.3 at. % sulfur, providing a concentration ratio of 1:2.1 for W/S, in good agreement with the existing literature.[38,54] XPS analysis of the NT post-TGA−MS confirms the chemical composition to be WO_3 with 15.0 at. % tungsten and 51.3 at. % oxygen being detected, correlating to a 1:3.3 ratio of W/O. Additionally, no sulfur was detected; indeed, no peaks were identified in the sulfur 2p region (Figure 6f), consistent with the TGA−MS data in that there was complete elimination of sulfur ions and oxidation of tungsten by heating the WS_2 NTs above 400 °C.

Specifically, Figure 6a,b shows the deconvoluted XPS spectra for W $4f_{7/2}$ and W $4f_{5/2}$ peaks at 32.5 and 34.7 eV and S $2p_{3/2}$ and S $2p_{1/2}$ peaks at 162.1 and 163.3 eV from WS_2, in agreement with the data reported in the literature.[55] From Figure 6a, small peaks from W $4f_{7/2}$ and W $4f_{5/2}$ WO_3 are also identified, attributed to the relatively high concentration of oxygen (7.3 at. %) detected in the NT sample. The associated peaks, clearly seen in Figure 6e, are derived from WO_3 obtained by heating the WS_2 NTs, which undergo complete oxidation to WO_3 nanostructures. The level of oxygen detected for the WS_2 NTs (19.9 at. %) is much less than that reported previously.[54] Additionally, significant amount of carbon is

detected for both the WS_2 NTs (20.0 at. %) and WO_3 (29.3 at. %) samples, Figure 6c,g, possibly associated with defects on the nanostructure surface or most likely from physisorption of hydrocarbons from atmospheric contamination as carbon is known to react and bind to the surface of tungsten atoms and is typically found loosely attached to the surface.[38,54,56,57]

SEM imaging of the pale yellow/ green powder exhibits collapse of 1D morphology of the WS_2 NTs and recrystallization into micron-sized 3D crystals of WO_3 due to the heating process. The NT structure (as seen in Figure 1) is no longer observed. These WO_3 structures were obtained by oxidation of the curved and cylindrical WS_2 NTs, collapse, and sintering of a few WO_3 crystals, resulting in diameters ranging from 0.5 to 3 μm (see Figure 7a). The image in Figure 7b shows the surface of the WO_3 particles to be cracked, a consequence of the WO_3 particles being annealed at the elevated temperatures used. Under these conditions, the WS_2 NTs are completely oxidized to WO_3 below 550 °C, and no further reaction occurs above this temperature.

In summary, WS_2 NTs are thermally stable up to at least 400 °C in air, a temperature well above that used to melt process most polymers and 0D/1D/2D nanoparticles. XPS, XRD, TGA−MS, and Raman data confirmed the structure of the NTs and the presence of oxygen and carbon contaminants most likely from the environment.

Given the potential medical and other applications where maintaining the molecular weight of the polymer is critical, for WS_2 NT-filled PLA, it is pertinent to assess if the oxygen and carbon moieties play any part in the thermal degradation of the polymer during melt mixing. To this end, the PLA and composites of PLA and WS_2 NTs, prior to and post-melt mixing in an extruder, were studied using GPC; see Supporting Information Figure S4. A reduction in the molecular weight (M_w) of the PLA and the composites is a measure of polymer degradation. A reduction in M_w could be due to the melt extrusion process or addition of the WS_2 NTs or other impurities to the PLA. The GPC curves shown in Figure S4a are recorded using the refractive index (RI) and light scattering (LS) detectors and display the molecular weight curves as a function of eluting time for the various materials. The RI and LS measurements for the PLA polymer samples were obtained within similar elution times, with only a small shift to higher elution time for the processed sample. This small shift in M_w values may indicate a low level of thermal-induced degradation due to processing. Figure S4b−S4d shows the molecular weight of samples determined using GPC computational software from the RI trace. The horizontal lines identify that the M_w of PLA pellets and dried PLA pellets before extrusion were $1.26 \pm 0.08 \times 10^5$ and $1.20 \pm 0.06 \times 10^5$ g/mol, respectively, highlighting the importance of drying the PLA before extrusion. The M_w of the unfilled PLA and composites of PLA and WS_2 NTs after melt extrusion was $1.1 \pm 0.05 \times 10^5$ g/mol. This small decrease of ∼0.2×10^5 g/mol after extrusion correlates with the shift seen in the RI and LS peaks identified in Figure S4a, again indicating that the processing procedure resulted in a small degree of PLA degradation. However, it also clearly shows that incorporation of WS_2 NTs does not impact the M_w of the PLA at any loading.

The dispersion of the NTs within the polymer post-melt extrusion was examined by SEM and STEM-BF imaging. SEM imaging of cross-sections of the fractured surfaces of the composite samples (Figure 7c) shows that individual NTs of 1−2 μm length are embedded and dispersed effectively within
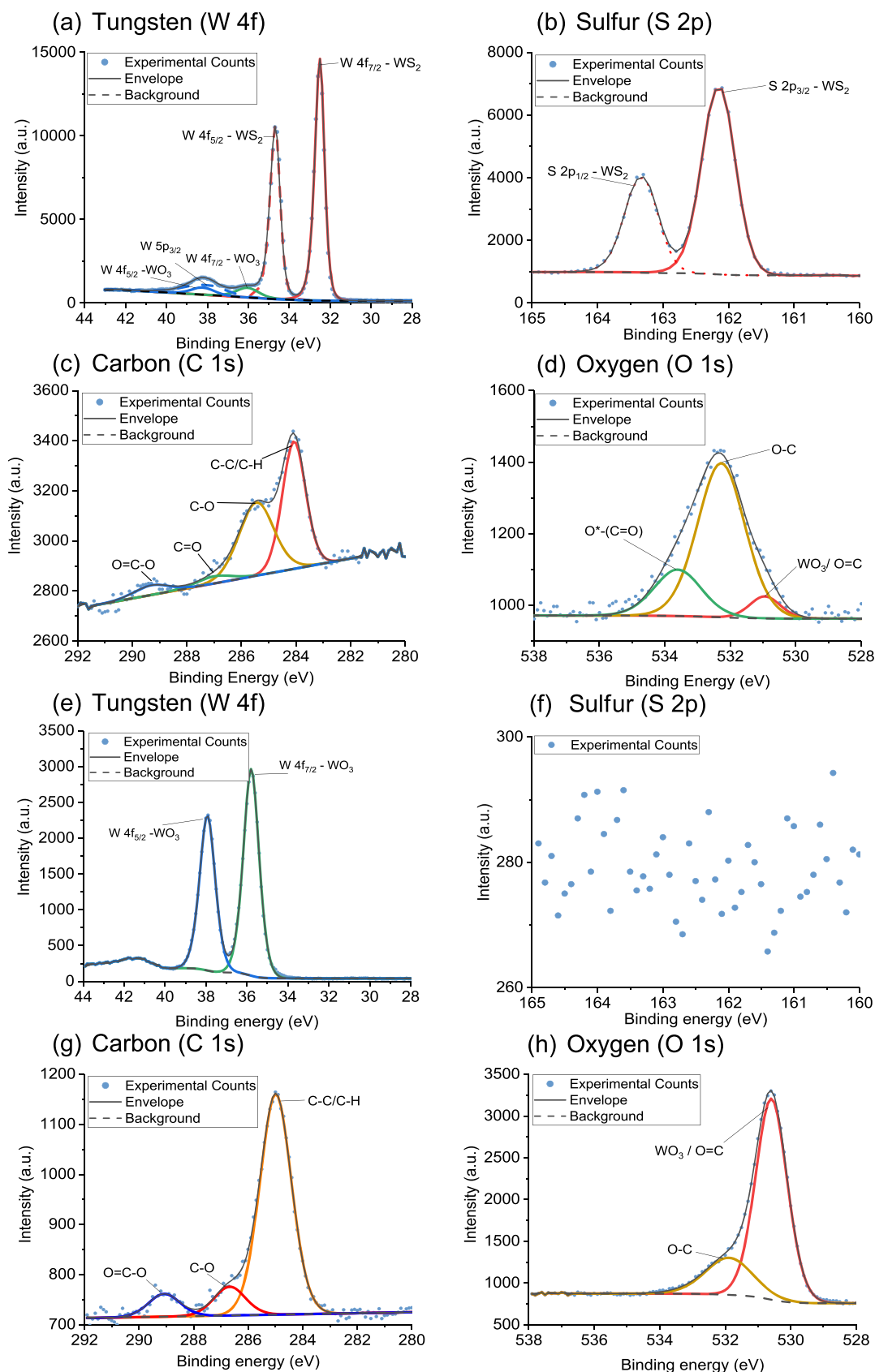
F

Figure 6. XPS analysis showing the deconvoluted spectra of WS$_2$ NTs (a−d) and WO$_3$ (e−h).

the PLA matrix. However, the length and therefore the AR of the NTs were significantly reduced post-melt processing (Figure 7d). Additionally, the NTs are both well dispersed

and distributed in the polymer. The STEM-BF images in Figure 7d−7g show that the NT lengths are in the range 200−800 nm post-processing. However, the diameters of the NTs
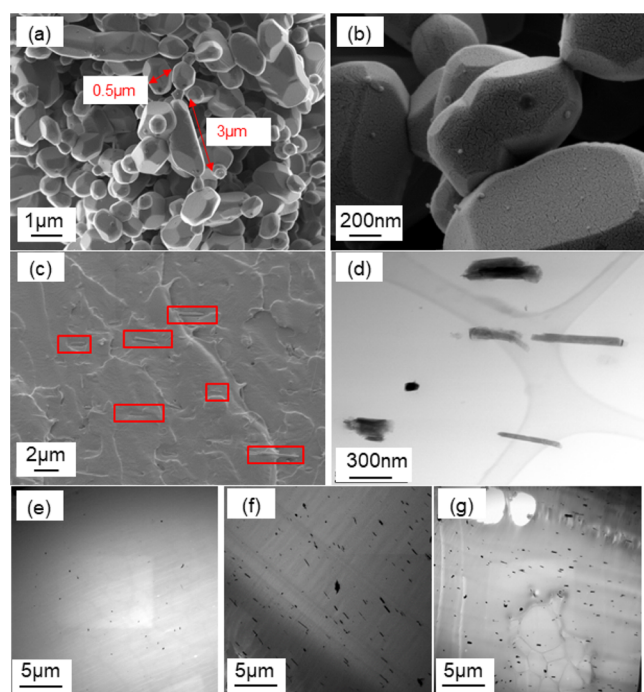
Figure 7. (a,b) SEM images of WO$_3$ particles obtained post-TGA–MS analysis of WS$_2$ NTs, (c) SEM image of a PLA composite with 3 wt % WS$_2$ NTs, (d) STEM-BF image of PLA 3.0 wt % WS$_2$, and (e–g) STEM-BF images of composites of PLA and 0.1, 0.5, and 3.0 wt % WS$_2$ NTs, respectively.

are much less affected by the extrusion process and are in a similar range, 30−100 nm, to that prior to processing. This significant reduction in the length (and thus the AR < 10) of the NTs is a consequence of the forces applied during mixing in a twin-screw extruder, resulting in substantial breakage of the NTs to lengths down to the sub-micron level. The shear stresses (forces) applied during melt mixing in the twin-screw extruder are sufficient to result in an approximate 95% plus reduction in the AR to <10, and this will significantly affect the quasi-static mechanical properties of these composites. The NT walls seem to be unravelled after the processing, and there is a catastrophic breakage of the NTs, see Figure 7d, resulting in a significant decrease in the AR of the NTs to ∼10. The shear stresses and extensional forces applied during melt mixing of PLA and the NTs induce a strain on the walls of NTs, causing the outer layers of the NTs to break. The shear modulus of the WS$_2$ NTs has been recently measured experimentally to be ∼70−80 GPa.[58]

From STEM-BF, the NTs, post-mixing, have widths of 70−110 nm and lengths of 100−300 nm; the latter are now significantly less than those prior to mixing. Consequently, although the NTs are highly dispersed in the PLA, their AR post-mixing is so small that they cannot contribute to the reinforcement of the polymer matrix. This is clearly seen from the tensile mechanical properties of the composites relative to the unfilled polymer as the Young's modulus (E), tensile strength (σ), and elongation at break (ε_b) of the PLA are slightly decreased or unchanged, within the experimental error, but a ∼30% decrease in tensile toughness was obtained; see Supporting Information Figure S5 and Table S1. Indeed, a similar behavior has just been reported for composites of poly(caprolactone) with another 1D filler, sepiolite needles;

the AR of the needles was low and reduced further as a consequence of melt mixing in a micro-compounder.[59]

Given that WS$_2$ NTs and many other nanofillers are known to have a strong nucleating effect on semicrystalline polymers, the crystallization behavior of PLA on addition of the NTs was studied using DSC, hot stage-polarized optical microscopy (POM), and WAXS/SAXS. From DSC measurements (Figure 8), the glass transition temperature (T_g), melting temperature
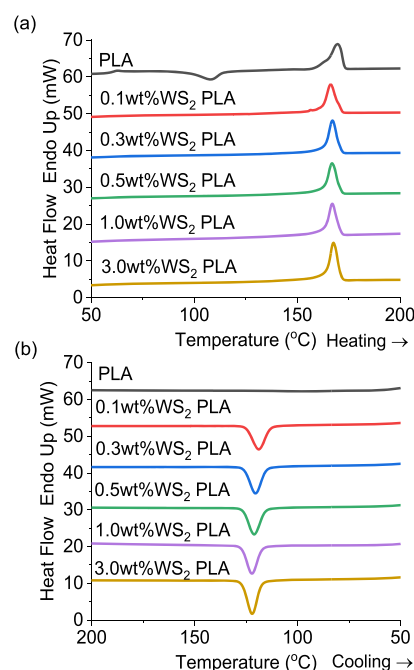

Figure 8. DSC (a) heating and (b) cooling curves of composites of PLA and WS$_2$ NTs in the 25−250 °C temperature range.

(T_m), enthalpy of melting (ΔH_m), crystallization temperature (T_c), enthalpy of crystallization (ΔH_c), and the percentage crystalline content (X_c) were determined, see Table 2. The addition of WS$_2$ NTs had no effect on the T_g and T_m of PLA; they remained essentially the same (∼59 and 168 °C, respectively) independent of NT concentration.

Table 2. Thermal Parameters Determined from DSC Measurements of Extruded PLA and Composites of PLA and WS$_2$ NTs

WS$_2$ NT (wt %)	T_g (°C)	T_m (°C)	ΔH_m (J/g)	T_c (°C)	ΔH_c (J/g)	X_c (%)
0	59	170	37			
0.1	60	166	39	119	41	44
0.3	60	167	39	121	40	43
0.5	59	167	39	121	42	45
1.0	59	167	37	122	42	44
3.0	59	168	43	122	45	47

Figure 8a shows the thermograms obtained after the second heating cycle; the melt-processed PLA sample exhibits a cold crystallization peak (T_{cc}) at 108 °C, in contrast to the composites, which do not show a T_{cc} peak at all. The identification of a T_{cc} peak indicates that the PLA sample was in a more amorphous state at RT with respect to the composites, and crystallization occurred during heating. Notably, the disappearance of the T_{cc} peak of PLA with the

addition of WS_2 NTs suggests a strong nucleating effect on PLA, inducing a higher degree of PLA crystallization.

Additionally, Figure 8b shows the cooling curves and the crystallization peak (T_c) of the composites clearly for all WS_2 NT loadings. However, PLA itself does not have an obvious T_c peak upon cooling, a behavior associated with the slow rate of crystallization of PLA. T_c of the PLA increased by ∼3 °C with increasing WS_2 NT loading but with a modest increase in crystallinity of 3.5%. However, these results demonstrate that the inclusion of the NTs alters the nucleation and crystallization behavior of the PLA.

The effective role of WS_2 NTs in promoting nucleation of PLA crystals was further studied by examining the composites under polarized light with an optical microscope equipped with a hot stage to investigate the rate of crystallization and crystal morphology as a function of WS_2 NT loading during heating and cooling cycles. The conditions chosen for the polarized light thermal cycles replicated the heating protocol used for the DSC measurements. Observation of the crystallization of unfilled PLA and composites of PLA and WS_2 NTs when cooling at a rate of 10 K min^{-1} confirmed the slow rate of crystallization of PLA (Figure 9). However, inclusion of WS_2 NTs into PLA results in the crystallization of PLA at a much higher rate (Figure 9b,c). Therefore, the sample was held at the temperature at which crystallization began, and the time taken for complete crystallization of the sample was recorded. For both unfilled PLA and the composites, the micrographs show that spherulite formation begins at 145 °C. Figure 9 shows the variation in spherulite morphology for unfilled PLA compared with the composites with up to 3 wt % WS_2 NT loading. For unfilled PLA (Figure 9a), significantly larger spherulites are formed due to the slower rate of crystallization and the longer time taken to complete spherulite growth, measured at 9 min. The spherulite size for the composites (Figure 9b,c) is much smaller and more densely populated. The WS_2 NTs act as nucleating points for crystallization of the PLA. The time taken for complete crystallization of the PLA with WS_2 NT loadings of up to 0.1 wt % Figure 9b) was approximately 45 s. However, at 3 wt % WS_2 NT loading, the time taken for complete crystallization increased to 2.25 min. This observation is associated with the more densely populated NTs at 3 wt %, making identification of the exact time for complete crystallization difficult to determine. However, it is clear that the inclusion of WS_2 NTs into this PLA has a significant impact on the crystallization kinetics and structure of the polymer.

WAXS and SAXS measurements were performed to further investigate the crystalline structure of extruded unfilled and WS_2 NT-filled PLA composites. The WAXS and SAXS 2D patterns and integrated 1D profiles were measured simultaneously and are shown in Figure 10.

The background intensity of the 2D profiles was subtracted, and the 1D WAXS (Figure 10a) intensities were normalized to the background to provide a better comparison of the relative intensities of the extruded samples. From the WAXS pattern (Figure 10a), the extruded PLA sample exhibits an amorphous halo also visible in the integrated 1D curve (Figure 10b) with no observable crystalline peaks. This result highlights the role that the extrusion process plays in generating a complete amorphous phase in the polymer that was initially crystalline (see the 2D pattern and integrated curve of the pellet, Figure 10a,b). The SAXS pattern of the extruded PLA shows no significant feature, while the PLA pellet pattern exhibits a clear
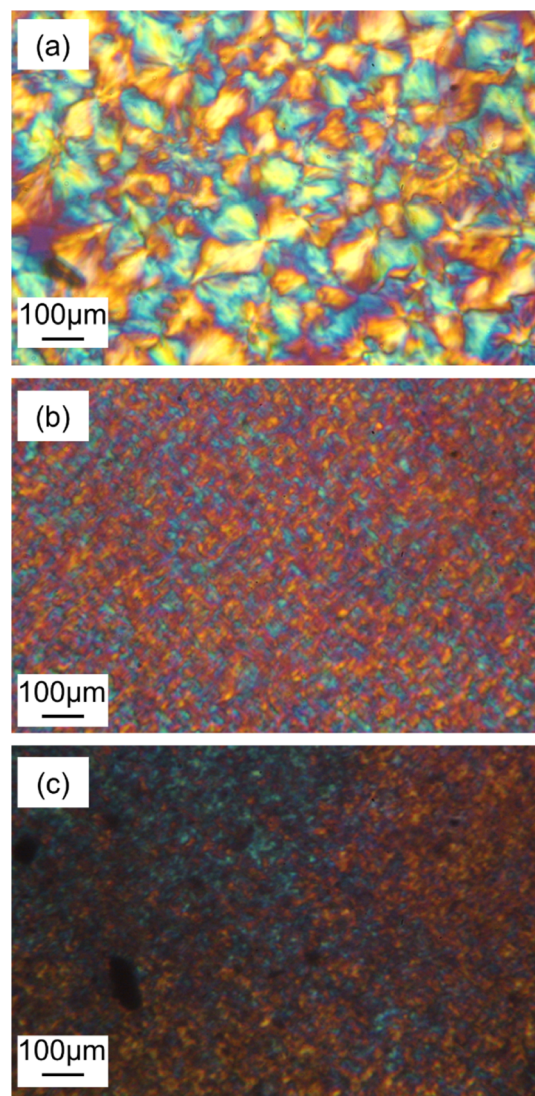

Figure 9. Complete crystal formation of (a) neat PLA at 9 min, (b) 0.1 wt % WS_2 NT filled PLA at 45 s, and (c) 3 wt % WS_2 NT-filled PLA at 2.25 min at 145 °C.

intensity ring (Figure 10c) that gives rise to a broad peak in the 1D integrated profile (Figure 10d). In the WAXS patterns of the WS_2 NTs composites, the WS_2 NT crystalline peaks are clearly identifiable; the main peak is attributed to the (002) reflection positioned at $q = 1.01$ Å^{-1}, which is in excellent agreement with the XRD analysis of the WS_2 NTs (Figure 5). The other peaks are attributed to the (004), (100), and (103) reflections of WS_2. The 1D WAXS profiles show a systematic increase in the intensity of the WS_2 peaks with increasing WS_2 NT loading. Moreover, a progressive reduction in the intensity of the amorphous halo until 15% for the composites with 3.0 wt % WS_2 NT loading in comparison to that of the extruded unfilled PLA indicates an increase in the overall PLA crystalline content, supporting the DSC results. Nevertheless, the crystalline domains formed in the nanocomposites are too small to give rise to a diffraction peak of PLA due to the strong nucleating effect of the WS_2 NTs (in agreement with the POM images in Figure 9).

The 1D SAXS profile for the composites with 1.0 and 3.0 wt % WS_2 NTs (Figure 10d) shows a saturation of the signal for q values below 0.0075 Å^{-1} due to the elevated scattering from
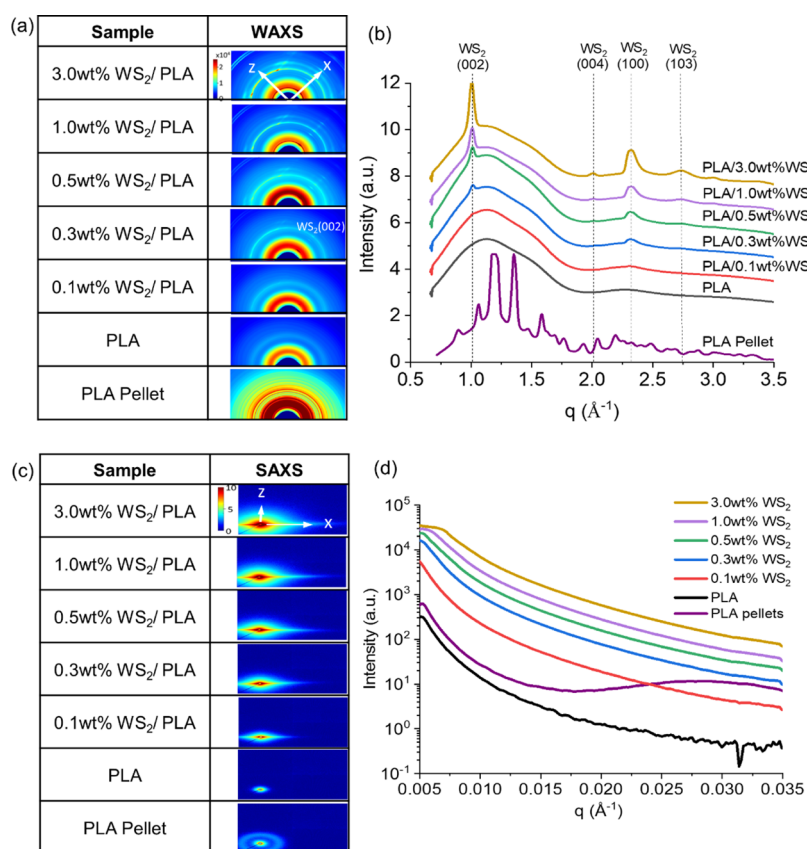
Figure 10. (a,b) WAXS 2D patterns and 1D integrated profiles and (c,d) corresponding SAXS 2D patterns and integrated 1D profiles for the as-purchased PLA pellet, extruded PLA, and composites of WS$_2$ NT and PLA.

the NTs at the higher concentrations. However, in the detector linear regime (above $q = 0.0075$ Å^{-1}), the signal is reliable and the increase in the scattering intensity with increasing WS$_2$ NTs loading is noticeable. It can be attributed to the high electron density of WS$_2$.

Moreover, consistent 1D profiles for all WS$_2$ NT loadings suggest an even dispersion and distribution of the NTs within the polymer matrix. This is further clarified from the 2D SAXS as the horizontally stretched pattern is suggestive of a homogenous alignment and distribution of WS$_2$ NTs with the PLA from extrusion.[60] This finding agrees with the NT alignment seen in the TEM images of the composites, while additionally generating ordering of the polymer chains. The inclusion of NTs provides surfaces from which the polymer can crystallize, confirming the role of WS$_2$ NTs as a nucleation agent for PLA.

4. CONCLUSIONS

Highly crystalline multi-walled (between 8 and 28 walls with a consistent wall spacing of 0.65 nm) WS$_2$ NTs having widths in the range 52−110 nm and lengths in the range 2.45−65.6 μm were synthesized using a new horizontal reactor. The WS$_2$ NTs were thermally stable in the air atmosphere up to 400 °C, while further heating in the region between 400 and 550 °C induced oxidation of tungsten via formation of SO$_2$/SO gas, resulting in the formation of yellow WO$_3$ micron-sized particles. The fact that the WS$_2$ NTs are thermally stable to at least 400 °C confirms that the NTs can be melt-mixed with polymers without thermally induced degradation. XPS and STEM−EDS analyses of the WS$_2$ NTs detected levels of oxygen and carbon,

known in this instance to be airborne contaminations, absorbed on a large surface area and inside the layers of tubular nanostructures.

As the surface of the WS$_2$ NTs was shown to be hydrophilic, they were readily dispersed and distributed in the PLA matrix by melt mixing, hitherto a method not widely used to prepare composites of WS$_2$ NTs and polymers in contrast to solution mixing. However, the shear stresses applied during twin-screw extrusion resulted in a significant chopping and therefore a reduction in the AR of the NTs of >95% to approximately 10, down to lengths between 200 and 800 nm. Consequently, the mechanical properties of the PLA were unchanged upon inclusion of the WS$_2$ NTs; the much-shortened chopped NTs provided no reinforcement. However, the much-shortened NTs did act as nucleating sites for PLA crystallization, resulting in an increased T_c for PLA with increasing WS$_2$ NT loading and a slightly higher degree of crystalline content. From POM experiments, a significant increase in the rate of crystallization at 145 °C from 9 min for extruded PLA to approximately 45 s for WS$_2$ NT-filled PLA at loadings <1 wt % was observed. WAXS/SAXS analysis identified a homogeneous distribution of WS$_2$ NTs in PLA post-extrusion. Extrusion was shown to produce a highly amorphous PLA (>99%) with no crystallinity, and therefore, the introduction of WS$_2$ NTs was effective in nucleating and inducing crystallization of the PLA. The decrease in the AR of the rigid 1D WS$_2$ NTs as a consequence of the high shear forces applied during melt mixing with PLA significantly reduces any possible mechanical reinforcement of the polymer for bioresorbable polymeric scaffolds applications.

■ ASSOCIATED CONTENT

Ⓢ Supporting Information

The Supporting Information is available free of charge at https://pubs.acs.org/doi/10.1021/acsanm.2c00489.

Schematic illustration of the synthesis of WS₂ NTs, TGA−MS analysis of WS₂ NTs as a function of temperature in an inert atmosphere (nitrogen), XPS survey spectra of WS₂ NTs before and after oxidation (i.e., WO₃), GPC analysis of PLA and WS₂ NT-filled PLA before and after extrusion, tensile testing results of composites of WS₂ NTs and PLA, and STEM−EDS data for WS₂ NTs (PDF)

■ AUTHOR INFORMATION

Corresponding Author

Tony McNally − *International Institute for Nanocomposites Manufacturing (IINM), WMG, University of Warwick, Coventry CV4 7AL, U.K.;* ⓞ orcid.org/0000-0001-5436-4211; Email: t.mcnally@warwick.ac.uk

Authors

Eimear Magee − *International Institute for Nanocomposites Manufacturing (IINM), WMG, University of Warwick, Coventry CV4 7AL, U.K.*

Fengzai Tang − *International Institute for Nanocomposites Manufacturing (IINM), WMG, University of Warwick, Coventry CV4 7AL, U.K.*

Esra Ozdemir − *International Institute for Nanocomposites Manufacturing (IINM), WMG, University of Warwick, Coventry CV4 7AL, U.K.*

Marc Walker − *Department of Physics, University of Warwick, Coventry CV4 7AL, U.K.*

Tiziana Di Luccio − *Division of Chemistry and Chemical Engineering, California Institute of Technology, Pasadena, California 91125, United States*

Julia A. Kornfield − *Division of Chemistry and Chemical Engineering, California Institute of Technology, Pasadena, California 91125, United States*

Alla Zak − *Physics Department, Faculty of Sciences, Holon Institute of Technology—HIT, Holon 5810201, Israel;* ⓞ orcid.org/0000-0002-3807-3454

Reshef Tenne − *Molecular Chemistry and Material Science, Weizmann Institute of Science, Rehovot 76100, Israel;* ⓞ orcid.org/0000-0003-4071-0325

Complete contact information is available at:
https://pubs.acs.org/10.1021/acsanm.2c00489

Notes

The authors declare no competing financial interest.

■ ACKNOWLEDGMENTS

■ REFERENCES

(1) Tenne, R.; Margulis, L.; Genut, M.; Hodes, G. Polyhedral and cylindrical structures of tungsten disulphide. *Nature* **1992**, *360*, 444.

(2) Margulis, L.; Salitra, G.; Tenne, R.; Talianker, M. Nested fullerene-like structures. *Nature* **1993**, *365*, 113−114.

(3) Zak, A.; Sallacan-Ecker, L.; Margolin, A.; Feldman, Y.; Popovitz-Biro, R.; Albu-Yaron, A.; Genut, M.; Tenne, R. Scaling Up of the WS2 Nanotubes Synthesis. *Fullerenes, Nanotub. Carbon Nanostruct.* **2011**, *19*, 18.

(4) Chithaiah, P.; Ghosh, S.; Idelevich, A.; Rovinsky, L.; Livneh, T.; Zak, A. Solving the "MoS2 Nanotubes" Synthetic Enigma and Elucidating the Route for Their Catalyst-Free and Scalable Production. *ACS Nano* **2020**, *14*, 3004−3016.

(5) Kaplan-Ashiri, I.; Cohen, S. R.; Gartsman, K.; Rosentsveig, R.; Seifert, G.; Tenne, R. Mechanical behavior of individual WS2 nanotubes. *J. Mater. Res.* **2004**, *19*, 454−459.

(6) Kaplan-Ashiri, I.; Cohen, S. R.; Gartsman, K.; Ivanovskaya, V.; Heine, T.; Seifert, G.; Wiesel, I.; Daniel Wagner, H.; Tenne, R. On the Mechanical Behavior of WS2 Nanotubes under Axial Tension and Compression. *Proc. Natl. Acad. Sci. U.S.A.* **2006**, *103*, 523.

(7) Višic, B.; Panchakarla, L. S.; Tenne, R. Inorganic Nanotubes and Fullerene-like Nanoparticles at the Crossroads between Solid-State Chemistry and Nanotechnology. *J. Am. Chem. Soc.* **2017**, *139*, 12865−12878.

(8) Deng, S.; Sumant, A. V.; Berry, V. Strain engineering in two-dimensional nanomaterials beyond graphene. *Nano Today* **2018**, *22*, 14−35.

(9) Gong, F.; Duong, H.; Papavassiliou, D. Review of Recent Developments on Using an Off-Lattice Monte Carlo Approach to Predict the Effective Thermal Conductivity of Composite Systems with Complex Structures. *Nanomaterials* **2016**, *6*, 142.

(10) Maharaj, D.; Bhushan, B. Characterization of nanofriction of MoS2 and WS2 nanotubes. *Mater. Lett.* **2015**, *142*, 207−210.

(11) Frey, G. L.; Tenne, R.; Matthews, M. J.; Dresselhaus, M. S.; Dresselhaus, G. Optical Properties of MS2 (M = Mo, W) Inorganic Fullerenelike and Nanotube Material Optical Absorption and Resonance Raman Measurements. *J. Mater. Res.* **1998**, *13*, 2412−2417.

(12) Sedova, A.; Khodorov, S.; Ehre, D.; Achrai, B.; Wagner, H. D.; Tenne, R.; Dodiuk, H.; Kenig, S. Dielectric and Electrical Properties of WS2 Nanotubes/Epoxy Composites and Their Use for Stress Monitoring of Structures. *J. Nanomater.* **2017**, *1*, 4838095.

(13) Pardo, M.; Shuster-Meiseles, T.; Levin-Zaidman, S.; Rudich, A.; Rudich, Y. Low Cytotoxicity of Inorganic Nanotubes and Fullerene-Like Nanostructures in Human Bronchial Epithelial Cells: Relation to Inflammatory Gene Induction and Antioxidant Response. *Environ. Sci. Technol.* **2014**, *48*, 3457−3466.

(14) Ramachandran, K.; Shao, Z.; Di Luccio, T.; Shen, B.; Bello, E. E. R.; Tammaro, L.; Villani, F.; Loffredo, F.; Borriello, C.; Di Benedetto, F.; Magee, E.; McNally, T.; Kornfield, J. A. Tungsten Disulfide nanotubes (WSNT) enhance flow-induced crystallization and radio-opacity of Polylactide (PLA) with without adversely affecting in vitro toxicity. *Acta Biomater.* **2022**, *138*, 313−326.

(15) Goldman, E. B.; Zak, A.; Tenne, R.; Kartvelishvily, E.; Levin-Zaidman, S.; Neumann, Y.; Stiubea-Cohen, R.; Palmon, A.; Hovav, A. H.; Aframian, D. J. Biocompatibility of tungsten disulfide inorganic nanotubes and fullerene-like nanoparticles with salivary gland cells. *Tissue Eng., Part A* **2015**, *21*, 1013−1023.

(16) Cheng, F.; Chen, J. Storage of hydrogen and lithium in inorganic nanotubes and nanowires. *J. Mater. Res.* **2006**, *21*, 2744−2757.

(17) Anju, S.; Mohanan, P. V. Biomedical applications of transition metal dichalcogenides (TMDCs). *Synth. Met.* **2021**, *271*, 116610.

(18) Katz, A.; Redlich, M.; Rapoport, L.; Wagner, H. D.; Tenne, R. Self-lubricating coatings containing fullerene-like WS2 nanoparticles for orthodontic wires and other possible medical applications. *Tribol. Lett.* **2006**, *21*, 135.

(19) Naffakh, M.; Maja, R.; Carlos, M.; Marián, A. G.-F.; Ignacio, J. Towards a new generation of polymer nanocomposites based on inorganic nanotubes. *J. Mater. Chem.* **2011**, *21*, 3574.

(20) Zohar, E.; Baruch, S.; Shneider, M.; Dodiuk, H.; Kenig, S.; Tenne, R.; Wagner, H. D. The Effect of WS2 Nanotubes on the

Properties of Epoxy-Based Nanocomposites. *J. Adhes. Sci. Technol.* **2011**, *25*, 1603.

(21) Silverman, T.; Naffakh, M.; Marco, C.; Ellis, G. Effect of WS2 Inorganic Nanotubes on Isothermal Crystallization Behavior and Kinetics of Poly(3-Hydroxybutyrate-co-3-hydroxyvalerate). *Polymers* **2018**, *10*, 166.

(22) Silverman, T.; Naffakh, M.; Marco, C.; Ellis, G. Morphology and thermal properties of biodegradable poly(hydroxybutyrate-co-hydroxyvalerate)/tungsten disulphide inorganic nanotube nanocomposites. *Mater. Chem. Phys.* **2016**, *170*, 145−153.

(23) Jamshidian, M.; Tehrany, E. A.; Imran, M.; Jacquot, M.; Desobry, S. Poly-Lactic Acid: Production, Applications, Nanocomposites. and Release Studies. *Compr. Rev. Food Sci. Food Saf.* **2010**, *9*, 552.

(24) Ju, J.; Peng, X.; Huang, K.; Li, L.; Liu, X.; Chitrakar, C.; Chang, L.; Gu, Z.; Kuang, T. High-performance porous PLLA-based scaffolds for bone tissue engineering: Preparation, characterization, and in vitro and in vivo evaluation. *Polymer* **2019**, *180*, 121707.

(25) Han, C.; Cai, N.; Chan, V.; Liu, M.; Feng, X.; Yu, F. Enhanced drug delivery, mechanical properties and antimicrobial activities in poly(lactic acid) nanofiber with mesoporous Fe3O4-COOH nanoparticles. *Colloids Surf., A* **2018**, *559*, 104−114.

(26) Choi, W. J.; Hwang, K. S.; Kwon, H. J.; Lee, C.; Kim, C. H.; Kim, T. H.; Heo, S. W.; Kim, J.-H.; Lee, J.-Y. Rapid development of dual porous poly(lactic acid) foam using fused deposition modeling (FDM) 3D printing for medical scaffold application. *Mater. Sci. Eng. C* **2020**, *110*, 110693.

(27) Ploypetchara, N.; Suppakul, P.; Atong, D.; Pechyen, C. Blend of Polypropylene/Poly(lactic acid) for Medical Packaging Application: Physicochemical, Thermal, Mechanical, and Barrier Properties. *Energy Proc.* **2014**, *56*, 201−210.

(28) Terzopoulou, Z.; Klonos, P. A.; Kyritsis, A.; Tziolas, A.; Avgeropoulos, A.; Papageorgiou, G. Z.; Bikiaris, D. N. Interfacial interactions, crystallization and molecular mobility in nanocomposites of Poly(lactic acid) filled with new hybrid inclusions based on graphene oxide and silica nanoparticles. *Polymer* **2019**, *166*, 1−12.

(29) Sharif, A.; Mondal, S.; Hoque, M. E. Polylactic Acid (PLA)-Based Nanocomposites: Processing and Properties. *Bio-based Polymers and Nanocomposites*; Springer: Cham, Switzerland, 2019.

(30) Raquez, J.-M.; Habibi, Y.; Murariu, M.; Dubois, P. Polylactide (PLA)-based nanocomposites. *Prog. Polym. Sci.* **2013**, *38*, 1504−1542.

(31) Shankar, S.; Wang, L.-F.; Rhim, J.-W. Incorporation of zinc oxide nanoparticles improved the mechanical, water vapor barrier, UV-light barrier, and antibacterial properties of PLA-based nanocomposite films. *Mater. Sci. Eng. C* **2018**, *93*, 289−298.

(32) Barmouz, M.; Behravesh, A. H. Statistical and experimental investigation on low density microcellular foaming of PLA-TPU/cellulose. nano-fiber bio-nanocomposites. *Polym. Test.* **2017**, *61*, 300−313.

(33) Chen, P.; Liang, X.; Xu, Y.; Zhou, Y.; Nie, W. Enhanced thermal and mechanical properties of PLA/MoS2 nanocomposites synthesized via the in-situ ring-opening polymerization. *Appl. Surf. Sci.* **2018**, *440*, 1143−1149.

(34) Mallick, S.; Ahmad, Z.; Touati, F.; Bhadra, J.; Shakoor, R. A.; Al-Thani, N. J. PLA-TiO2 nanocomposites: Thermal, morphological, structural, and humidity sensing properties. *Ceram. Int.* **2018**, *44*, 16507−16513.

(35) Salahuddin, N.; Abdelwahab, M.; Gaber, M.; Elneanaey, S. Synthesis and Design of Norfloxacin drug delivery system based on PLA/TiO2 nanocomposites: Antibacterial and antitumor activities. *Mater. Sci. Eng. C* **2020**, *108*, 110337.

(36) Ghosh, S.; Otorgust, G.; Idelevich, A.; Regev, O.; Lapsker, I.; Lewitus, D. Y.; Zak, A. Reinforcement of poly (methyl methacrylate) by WS2 nanotubes towards antiballistic applications. *Compos. Sci. Technol.* **2021**, *207*, 108736.

(37) Haba, D.; Griesser, T.; Müller, U.; Brunner, A. Comparative investigation of different silane surface functionalizations of fullerene-like WS2. *J. Mater. Sci.* **2015**, *50*, 5125.

(38) Chen, Y.; Deniz, H.; Qin, L.-C. Accurate measurement of the chirality of WS2 nanotubes. *Nanoscale* **2017**, *9*, 7124−7134.

(39) Remškar, M.; Mrzel, A. High-temperature fibres composed of transition metal inorganic nanotubes. *Curr. Opin. Solid State Mater. Sci.* **2004**, *8*, 121−125.

(40) Martínez, J. I.; Laikhtman, A.; Moon, H. R.; Zak, A.; Alonso, J. A. Modelling of adsorption and intercalation of hydrogen on/into tungsten disulphide multilayers and multiwall nanotubes. *Phys. Chem. Chem. Phys.* **2018**, *20*, 12061−12074.

(41) Schuffenhauer, C.; Wildermuth, G.; Felsche, J.; Tenne, R. How stable are inorganic fullerene-like particles? Thermal analysis (STA) of inorganic fullerene-like NbS2, MoS2, and WS2 in oxidizing and inert atmospheres in comparison with the bulk material. *Phys. Chem. Chem. Phys.* **2004**, *6*, 3991−4002.

(42) Sekine, T.; Nakashizu, T.; Toyoda, K.; Uchinokura, K.; Matsuura, E. Raman scattering in layered compound 2H-WS2. *Solid State Commun.* **1980**, *35*, 371−373.

(43) Staiger, M.; Rafailov, P.; Gartsman, K.; Telg, H.; Krause, M.; Radovsky, G.; Zak, A.; Thomsen, C. Excitonic resonances in WS 2 nanotubes. *Phys. Rev. B: Condens. Matter Mater. Phys.* **2012**, *86*, 165423.

(44) Grinberg, O.; Deng, S.; Zussman, E.; Livneh, T.; Zak, A. Raman scattering from single WS2 nanotubes in stretched PVDF electrospun fibers. *Phys. Chem. Chem. Phys.* **2017**, *19*, 18443−18451.

(45) Tenne, R.; Redlich, M. Recent progress in the research of inorganic fullerene-like nanoparticles and inorganic nanotubes. *Chem. Soc. Rev.* **2010**, *39*, 1423−1434.

(46) Berkdemir, A.; Gutiérrez, H. R.; Botello-Méndez, A. R.; Perea-López, N.; Elías, A. L.; Chia, C.-I.; Wang, B.; Crespi, V. H.; López-Urías, F.; Charlier, J.-C.; Terrones, H.; Terrones, M. Identification of individual and few layers of WS2 using Raman Spectroscopy. *Sci. Rep.* **2013**, *3*, 1755.

(47) Daniel, M. F.; Desbat, B.; Lassegues, J. C.; Gerand, B.; Figlarz, M. Infrared and Raman study of WO3 tungsten trioxides and WO3.xH2O tungsten trioxide tydrates. *J. Solid State Chem.* **1987**, *67*, 235−247.

(48) Thakur, A. K.; Mukta, V. L.; Rakshit, S.; Koustav, N. M.; Gupta, V.; Parul, K. S.; Shashi, B. S. Controlled synthesis of WO3 nanostructures: optical. structural and electrochemical properties. *Mater. Res. Express* **2019**, *6*, 025006.

(49) Kopnov, F.; Tenne, R.; Späth, B.; Jägermann, W.; Cohen, H.; Feldman, Y.; Zak, A.; Moshkovich, A.; Rapoport, L. X-Ray Photoelectron Spectroscopy and Tribology Studies of Annealed Fullerene-like WS2 Nanoparticles. *Functionalized Nanoscale Materials, Devices and Systems*; Springer Netherlands: Dordrecht, 2008; pp 51−59.

(50) Liang, F.; Zhu, Y.; Liu, Y.; Han, D. Carbon nanotubes decorated with gold nanoparticles. *Nanomed. Nanotechnol. Biol. Med.* **2018**, *14*, 1788.

(51) Sedova, A.; Leitus, G.; Feldman, Y.; Bendikov, T.; Popovitz-Biro, R.; Khodorov, S.; Dodiuk, H.; Kenig, S.; Tenne, R. Synthesis of magnetic FeWO4 nanoparticles and their decoration of WS2 nanotubes surface. *J. Mater. Sci.* **2017**, *52*, 6376−6387.

(52) Rothschild, A.; Popovitz-Biro, R.; Lourie, O.; Tenne, R. Morphology of Multiwall WS2 Nanotubes. *J. Phys. Chem. B* **2000**, *104*, 8976−8981.

(53) Piskunov, S.; Lisovski, O.; Zhukovskii, Y. F.; D'yachkov, P. N.; Evarestov, R. A.; Kenmoe, S.; Spohr, E. First-Principles Evaluation of the Morphology of WS2 Nanotubes for Application as Visible-Light-Driven Water-Splitting Photocatalysts. *ACS Omega* **2019**, *4*, 1434.

(54) Višic, B.; Cohen, H.; Popovitz-Biro, R.; Tenne, R.; Sokolov, V. I.; Abramova, N. V.; Buyanovskaya, A. G.; Dzvonkovskii, S. L.; Lependina, O. L. Direct Synthesis of Palladium Catalyst on Supporting WS2 Nanotubes and its Reactivity in Cross-Coupling Reactions. *Chem.—Asian J.* **2015**, *10*, 2234−2239.

(55) Morgan, D. J. Core-level spectra of powdered tungsten disulfide, WS2. *Surf. Sci. Spectra* **2018**, *25*, 014002.

(56) Tsverin, Y.; Popovitz-Biro, R.; Feldman, Y.; Tenne, R.; Komarneni, M. R.; Yu, Z.; Chakradhar, A.; Sand, A.; Burghaus, U.

Synthesis and characterization of WS2 nanotube supported cobalt catalyst for hydrodesulfurization. *Mater. Res. Bull.* **2012**, *47*, 1653−1660.

(57) lu, Z.; Kanan, S. M.; Tripp, C. P. Synthesis of high surface area monoclinic WO3 particles using organic ligands and emulsion based methods. *R. Soc. Chem.* **2002**, *12*, 983−989.

(58) Nagapriya, K. S.; Goldbart, O.; Kaplan-Ashiri, I.; Seifert, G.; Tenne, R.; Joselevich, E. Torsional Stick-Slip Behavior in WS(2) Nanotubes. *Phys. Rev. Lett.* **2008**, *101*, 195501.

(59) Eriksson, M.; Goossens, H.; Peijs, T. Influence of the Solidification Process on the Mechanical Properties of Solid-State Drawn PCL/Sepiolite Nanocomposite Tapes. *Fibers* **2020**, *8*, 70.

(60) Rocher, L.; Ylitalo, A. S.; Di Luccio, T.; Miscioscia, R.; De Filippo, G.; Pandolfi, G.; Villani, F.; Zak, A.; Menary, G. H.; Lennon, A. B.; Kornfield, J. A. Interaction of Poly L-Lactide and Tungsten Disulfide Nanotubes Studied by In Situ X-ray Scattering during Expansion of PLLA/WS2NT Nanocomposite Tubes. *Polymers* **2021**, *13*, 1764−1783.